Luminescence of ZnO nanocrystals in silica synthesized by dual (Zn, O) implantation and thermal annealing

OPEN ACCESS
IOP Publishing
Journal of Physics D: Applied Physics
J. Phys. D: Appl. Phys. **54** (2021) 265104 (9pp)
https://doi.org/10.1088/1361-6463/abf0ec

Luminescence of ZnO nanocrystals in silica synthesized by dual (Zn, O) implantation and thermal annealing

I Parkhomenko[1], L Vlasukova[1], F Komarov[2,3], M Makhavikou[2], O Milchanin[2], E Wendler[4,*], M Zapf[4] and C Ronning[4]

[1] Belarusian State University, Minsk, Belarus
[2] A.N. Sevchenko Research Institute of Applied Physics Problems of Belarusian State University, Minsk, Belarus
[3] National University of Science and Technology MISIS, Moscow, Russia
[4] Institute for Solid State Physics, Friedrich-Schiller-University Jena, Jena, Germany

E-mail: elke.wendler@uni-jena.de

Received 1 December 2020, revised 23 February 2021
Accepted for publication 22 March 2021
Published 20 April 2021

Abstract

Zinc blende ZnO nanocrystals (NCs) were synthesised in amorphous silica by high-fluence dual (Zn, O) ion implantation and subsequent thermal annealing in air. We observed the formation of core/shell nanoparticles at the depth of maximum Zn concentration as a result of an incomplete oxidation process. The silica matrix with ZnO NCs exhibits an intense white-greenish emission. Low-temperature photoluminescence spectroscopy revealed various radiative recombination mechanisms in the zinc blende ZnO NCs involving intrinsic defects that act as donors and acceptors.

Keywords: zinc blende ZnO, nanocrystals, photoluminescence, bound exciton, intrinsic defects

(Some figures may appear in colour only in the online journal)

1. Introduction

Nanostructures of ZnO have recently attracted great attention due to their unique semiconducting, optical, piezoelectric and pyroelectric properties. Such nanostructures should be embedded in a transparent matrix such as silica, glass or Al_2O_3 in order to develop novel nanoscale ZnO-based devices. This has been successfully realised using either sol–gel techniques [1–3], reactive magnetron sputtering [4] or ion beam synthesis [5–8]. The latter has some advantages. As a clean process, ion implantation provides a high chemical stability of the synthesised nanocomposites as well as the possibility to control concentration and depth of the embedded nanoparticles. In addition, ion implantation is fully compatible with the current semiconductor technology.

To date, various regimes of ion implantation and subsequent annealing of implanted layers were investigated for the synthesis of Zn, ZnO and Zn_2SiO_4 nanostructures [5–8]. However, there are still a number of unclear points concerning the defect states in the synthesised nanoclusters. During ion beam synthesis, the growth and, in turn, the defect composition of the synthesised clusters are affected by various effects such as the post-implantation annealing regime, the concentration of the implanted species and their interaction with the matrix. The knowledge on the defect types and their role in carrier recombination processes is important for future optoelectronic and spintronic applications of ion-beam synthesised ZnO nanocrystals (NCs). Low-temperature photoluminescence (PL) is a powerful method for the analysis

* Author to whom any correspondence should be addressed.

of radiative defect levels and thus may yield information about the defect structure. However, there are only a few reports on low-temperature PL of ZnO NCs, ion-beam synthesised in silica [6, 7]. In this study, we report on the fabrication of ZnO NCs in silica by dual (Zn, O) ion implantation and subsequent thermal annealing. Low temperature PL spectroscopy has been applied to reveal the radiative recombination mechanisms in the synthesised ZnO NCs.

2. Experimental

The initial SiO_2/Si samples were cut from thermally oxidized Si-substrates. The thickness of the SiO_2 layer, as measured by transmission electron microscopy in cross-section geometry, was about 600 nm. These samples were implanted at nominal room temperature with 140 keV-Zn ions to the fluence of 5×10^{16} cm^{-2} and 50 keV-O ions to the fluence of 5×10^{16} cm^{-2}. Afterwards, the samples were annealed at 750 °C for 120 min in air ambient.

The relative concentration of Zn atoms versus depth (Zn distributions) in the implanted and annealed samples was obtained by Rutherford backscattering spectroscopy (RBS) using 1.8 MeV He^+ ions. The Zn distributions were extracted by fitting calculated RBS spectra to the experimental ones using the code SIMNRA [9]. For comparison the Zn depth profile was calculated with SRIM-2013 [10]. The structural investigations and phase analysis of the annealed sample were carried out using TEM in plan-view geometry as well as selected area electron diffraction (SAED). A Hitachi H-800 analytical electron microscope operating at 200 keV was used for these studies. Specimens for TEM research were prepared by a conventional technique that included precision cutting, cutting wheels, grinding, polishing and ion polishing using the Gatan equipment. In the finishing treatment, low energetic Ar^+ ions (3–5 keV) at sliding etching angles (3–5°) were used, to prevent or minimise the introduction of structural defects into the samples during their preparation.

PL spectra were recorded at low (4 K) and room temperature using the 3.81 eV (325 nm) emission line of a continuous wave He–Cd laser for excitation in a self-built PL system [11]. The beam diameter is determined by an iris aperture which helps for a reproducible adjustment of the laser beam. The excitation laser light is guided by mirrors through a pellin–broca prism to separate the excitation wavelength from other harmonics. A part of the laser beam is guided by a beam splitter to a power diode for on-line monitoring. The dispersed PL is detected by a CCD. The power of excitation and accumulation time were 213 mW and 60 s, respectively.

3. Results and discussion

Figure 1 shows the RBS spectra and the extracted Zn depth profiles. Oxygen concentration profiles cannot be determined from the measured RBS spectra, because of the low backscattering yield for this light element. For the as-implanted sample, the zinc depth profile is in reasonable agreement with that obtained from SRIM calculations. The zinc concentration

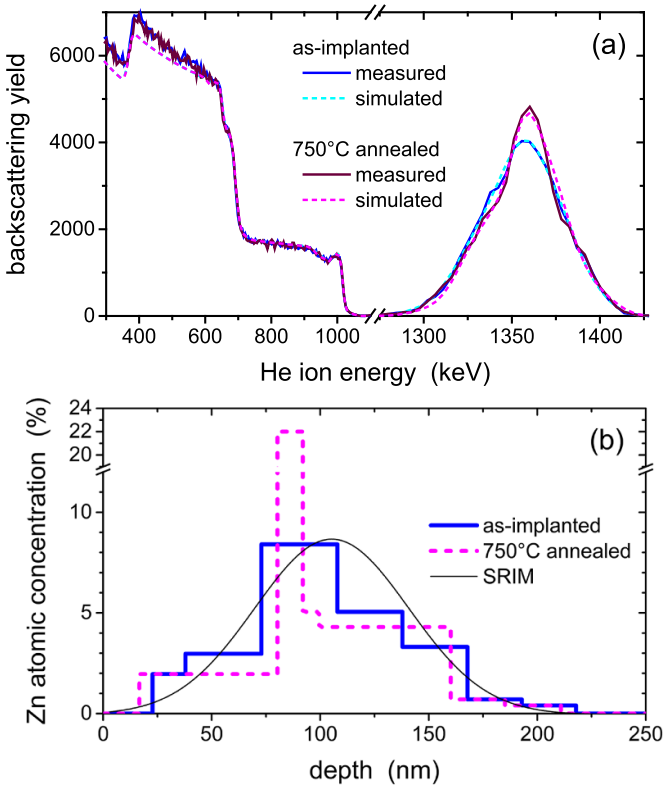

Figure 1. Energy spectra of backscattered He ions (a) and relative concentration of Zn atoms (given in at. %) versus depth (b) in SiO_2/Si after implantation of Zn and O ions with each 5×10^{16} cm^{-2} and annealing at 750 °C for 2 h in air. The Zn distribution calculated with SRIM is given as thin black line for comparison (for details see text).

maximum of about 8% is located at depths of 70…110 nm. Subsequent annealing (750 °C, 120 min) resulted in a redistribution of Zn atoms towards the centre of the profile. The total amount of Zn is accounted to be 4.7×10^{16} cm^{-2} and did not change after annealing.

After ion implantation, only small zinc-containing clusters formed with a diameter of 2–5 nm (not shown). Reflections from the crystalline phase were not recorded in the electron diffraction patterns. This indicates either the amorphous structure of these precipitates or the number of crystallites is very small—below the sensitivity limit of the method. Figure 2 shows plan-view TEM images and a corresponding SAED pattern of the silica subsurface region (at the depth of 0–100 nm) after ion implantation and annealing. Small precipitates with a rounded shape and diameter of 7–8 nm are observed on bright-field TEM images. The SAED pattern shows thin rings. The analysis of the dark-field TEM-image and SAED pattern indicates that the observed precipitates are crystalline. To identify the synthesised precipitates, the interplanar distances d_{HKL} have been calculated from the diameter D of the rings in the SAED pattern by

$$d_{HKL} = C/D, \tag{1}$$

$$C = d_T \times D_T = d_x \times D_x \tag{2}$$

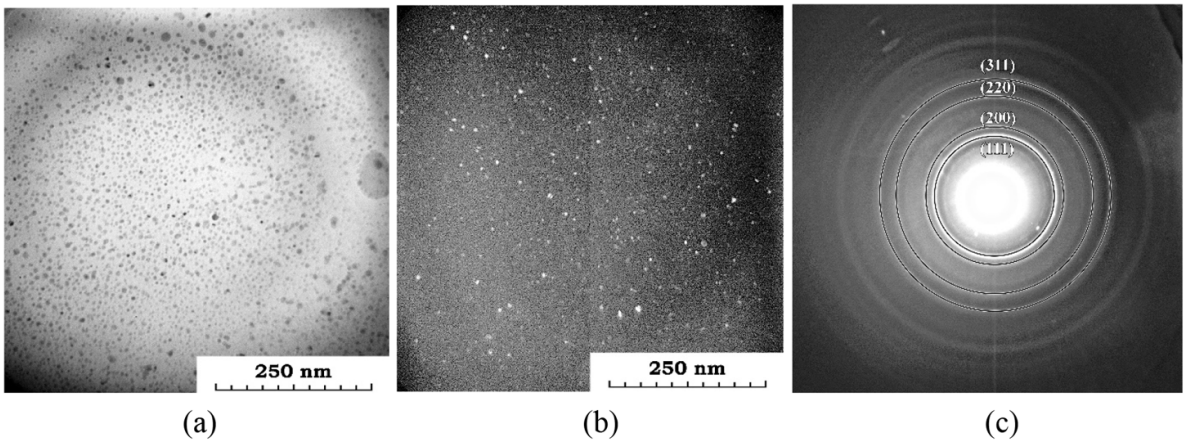

Figure 2. Bright-field (a), dark-field (b) TEM images and SAED pattern (c) of the silica layer after implantation of Zn and O ions with each 5×10^{16} cm^{-2} and annealing at 750 °C for 2 h in air.

$$d_x = d_R \times D_R / D_x \tag{3}$$

$$a^2 = \left(H^2 + K^2 + L^2\right) \cdot d^2_{HKL} \tag{4}$$

$$Q_x = d_{1HKL}^2 / d_{xHKL}^2 = \left(H_x{}^2 + K_x{}^2 + L_x{}^2\right) / \left(H_1{}^2 + K_1{}^2 + L_1{}^2\right) \tag{5}$$

where $C = L \times \lambda$ is the microscope constant, λ is the electron wavelength, L is the distance from the sample to the plane of the electron diffraction pattern registration, a is the lattice parameter, D_x is the diameter of the ring in the electron diffraction pattern, d_T and D_T are the corresponding distances for the test sample (polycrystalline Au thin film). Q_x is a row of values used to calculate interplanar parameters of crystalline materials with a cubic lattice (it follows from equation (4)). The calculation data are summarized in table 1. The data given in this table prove the formation of ZnO NCs with a cubic face-centered type of crystalline lattice. This follows from the practically complete coincidence of the Q_x-series obtained from experimental (column 4) and calculated values (column 7). There are two metastable modifications of the cubic ZnO phase: sphalerite or zinc blende (zb-ZnO [12]) and rock salt (rs-ZnO [13]). In our experiment the reflections from the (222), (400) and (420) planes for the cubic lattice are not registered, which is in good agreement with the formation of the sphalerite phase for binary compounds, in contrast to the rock salt lattice. Thus, the ZnO precipitates synthesised in silica are identified as crystallites of a face-centred cubic phase with a sphalerite type structure (F-43 m symmetry type). It should be noted that zinc blende materials are more suitable for applications in semiconductor technology due to the lower ionicity compared to that of the wurtzite materials. The advantages of zb-ZnO are also a lower carrier scattering, the existence of piezoelectric polarization, the absence of piezoelectric field effect and a larger dielectric constant compared with the wurtzite ZnO phase [14]. The lattice parameter of the ZnO cubic phase was calculated using equation (4) for all planes fixed in the SAED pattern (column 8 in table 1). The average lattice parameter calculated is 3.63 ± 0.03 Å. It is much less in comparison with values of the lattice parameter reported in literature. The zinc oxide phase with sphalerite structure is a metastable one, and ZnO single crystals with zinc blende structure have not been obtained up to now [12]. This phase is stabilized upon heteroepitaxial growth of ZnO films on substrates with a cubic structure (ZnS, GaAs/ZnS, SiO_2/Si) [12] or upon electrochemical ZnO deposition into SiO_2/Si track templates [15]. The reported values of the lattice constant vary from 4.37 to 4.62 Å.

Figure 3 shows TEM-images of precipitates in the implanted and annealed silica taken at a deeper region near the mean projected range R_p of the implanted Zn ions. Small precipitates with diameters ranging from 2 to 8 nm are formed in depths above and below R_p. Single bigger precipitates with sizes from 35 to 50 nm are located at depths around R_p. Some of these large precipitates are characterized by a faceted shape (figure 3(b)). There are secondary defects (mainly twin boundaries) inside of faceted precipitates. Additionally, one can see precipitates with core/shell structure in this region (marked by arrows in figure 3(b)). The contrast between cores and shells of the NCs becomes more prominent with further magnification. A SAED pattern was not taken from this region. However, we can assume that such precipitates are composed by a Zn core (darker contrast) and a ZnO shell (lighter contrast) in figures 3(b)–(d).

In the following, a possible scenario is discussed for the precipitation process in our experiment. At first, the formation of a Zn super-saturated layer in silica during high-fluence Zn implantation results in a subsequent impurity precipitation. Amekura *et al* reported the formation of Zn NCs in silica after high-fluence Zn^+ implantation in a similar regime as in our experiment [16]. The enthalpy of oxide formation is quite low for zinc [17]. Hence, zinc oxidizes easily when it comes in contact with oxygen. In our experiment this is the case due to the subsequent O ion implantation and the post-implantation annealing in oxidizing ambient. We can suppose that small Zn precipitates transform completely in ZnO ones in the regions of silica located above and below the R_p area. According to the

Table 1. Calculation of the crystal lattice parameters for zb-ZnO nanocrystals formed in silica by Zn and O ions implantation and subsequent annealing at 750 °C for 120 min at air ambient.

Experimental data (calculated from SAED pattern)				Modelling of parameters for a face-centred cubic lattice			Calculation of lattice parameters (equation (4)) taking into account the values of columns 3 and 6	
Electron diffraction ring number, x	Calculation of interplanar distances (equation (3)) using a test sample, d_x, Å	$d^2{}_x$, Å^2	$Q_x = {d_1}^2{}_{HKL}/{d_x}^2{}_{HKL}$	HKL	$H^2 + K^2 + L^2$	$Q_x = ({H_x}^2 + {K_x}^2 + {L_x}^2)/({H_1}^2 + {K_1}^2 + {L_1}^2)$	a, Å	$\Delta a = (a\text{-}a_{\text{average}})$, Å
1	2	3	4	5	6	7	8	9
1	2.105	4.4310	1.000	111	3	1.000	3.646	−0.006
2	1.828	3.3416	1.326	200	4	1.333	3.656	+0.004
3	1.294	1.6744	2.646	220	8	2.666	3.660	+0.008
4	1.099	1.2078	3.669	311	11	3.666	3.645	−0.007
				222	12	4.000		
				400	19	6.333		
5	0.823	0.6773	6.542	331	19	6.333	3.587	−0.065
				420	20	6.666		
6	0.741	0.5491	8.070	422	24	8.000	3.630	−0.022
				333	27	9.000		
7	0.695	0.483	9.174	511	27	9.000	3.611	−0.041

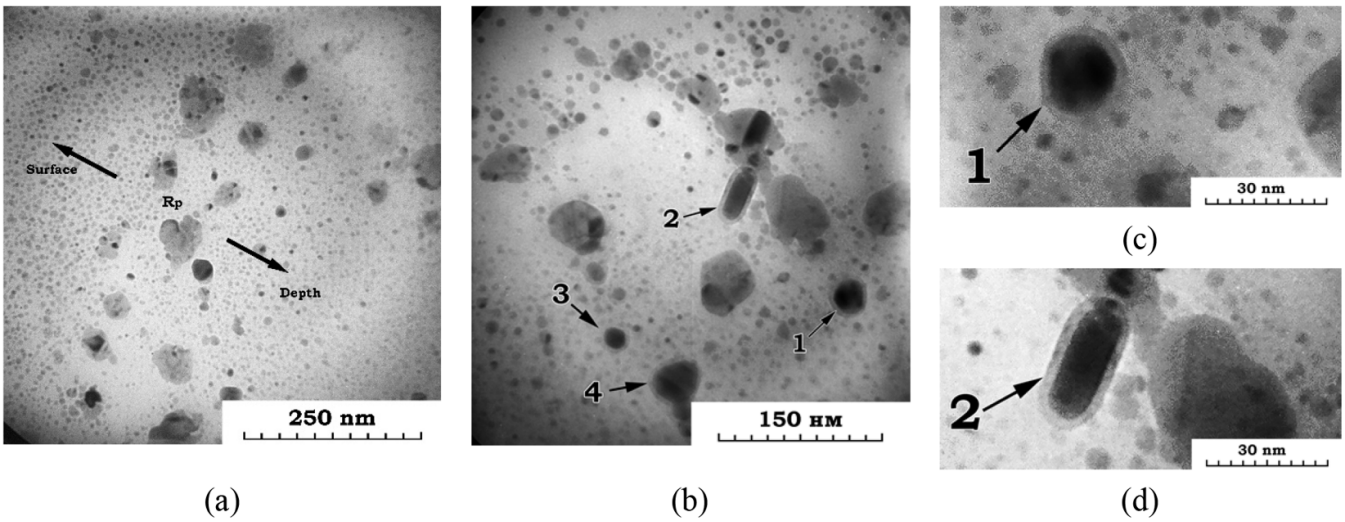

Figure 3. Bright-field TEM images of precipitates in silica after implantation of Zn and O ions with each 5×10^{16} cm^{-2} and annealing at 750 °C for 2 h in air. The images are taken at a depth near the mean projected range of Zn and O ions. Parts (c) and (d) depict enlarged images of core/shell precipitates.

RBS data, the concentration of Zn around the R_p area amounts to ∼8 at.%. This is an extremely high level of supersaturation, and big Zn precipitates are formed in this region of silica. Diffusion of both zinc (out of Zn clusters) and oxygen (into Zn clusters) contributes to the growth of an oxide shell. However, Zn and O diffusion becomes negligible and oxide growth stops after reaching a certain limiting thickness of the oxide shell [18]. If Zn precipitates are bigger than 15 nm it results in the formation of Zn core/ZnO shell precipitates [17] as in our case.

Before we start the discussion of the luminescent properties of the synthesised material, a brief overview of acclaimed features of zb-ZnO luminescence is given. Owing to the fact that ZnO has a similar ion stacking in both wurtzite and zinc blende symmetries, optical properties, in particular luminescence, of zinc blende and wurtzite ZnO are similar [19]. However, the piezoelectric field effect usually quenches the exciton energies in the wurtzite phase. This effect is absent in the zinc blende structure, and we can expect a stronger emission stimulated by excitons in this case [13]. Theoretical and experimental values of the band gap of zb-ZnO vary from 3.08 to 3.26 eV [20–23]. The near band edge (NBE) maximum emission at room temperature was observed at 3.1 eV for zb-ZnO nanorod arrays [24], 3.17 eV for zb-ZnO films [25], 3.26 eV for zb-ZnO layers [26] and at 3.368 eV for zb-ZnO epilayers [27]. It was shown in [18]. that additional bands appear in the PL spectra of the cubic zinc blende films in addition to the wurtzite-characteristic bands. According to [14, 25, 28] the photon energy difference between the zinc blende and wurtzite ZnO band-gap or NBE PL lines are found to be between 30 and 100 meV. Therefore, the clarification of the PL spectra of zb-ZnO nanostructures can be based on data for the well-analysed ZnO wurtzite. It also should be noted that frequencies of vibrational modes for the cubic modification nearly coincide with those of the hexagonal phase [29]. Longitudinal (LO) and transverse (TO) optical phonon energies in the zb-ZnO phase are ∼69 meV and ∼50 meV, respectively [30]. So, the manifestation of phonon replicas of PL bands is to be expected in the spectra.

The PL spectrum of the as-implanted sample registered at room temperature exhibits two weak bands with maxima at 2.56 and 1.9 eV (not shown here) most likely related to radiative defects in the silica matrix. Annealing results in an increase of the PL intensity by four times. Figure 4(a) depicts the room-temperature PL (RT PL) spectrum of the implanted and annealed sample which exhibits a weak UV band, broad emission in the green-blue range (2.3–2.8 eV) and a dominating band with the maximum in the yellow range (2.16 eV). Apparently, the observed emission is a combination of emission lines from ZnO and silica. The PL spectrum exhibits the ZnO NBE UV emission, which is located around 3.244 eV (see inset of figure 4(a)). It can be attributed to free (FE) or bound excitons (BX). Interestingly, a second weak band has been revealed in the UV range with the maximum at 3.189 eV (see inset in figure 4(a)). This band cannot be attributed to a phonon replica of the exciton-related band at 3.244 eV, because the energy difference of 55 meV between these bands is less than the energy of the LO optical phonon in ZnO. As will be shown below, the origin of the band at 3.189 eV is most likely related to the acceptor bound exciton (ABX). The emission in the broad visible region from 1.5 to 3 eV seems to be a combination of the deep level emission of ZnO and radiative transitions of defects in silica (see e.g. [31] and references therein). Under the assumption that ZnO NCs are the main source of emission, the broad emission at 2.3–2.8 eV as well as the dominant band at 2.16 eV can be attributed to intrinsic defects inside the ZnO nanoparticles [32]. The origin of the visible emission of ZnO nanostructures is still controversial because of the existence of complicated microscopic defects in ZnO. There are many attempts to correlate specific components of the emission with the presence or deficiency of various specific native defects [33, 34]. Taking into account literature data [3, 33, 35] and

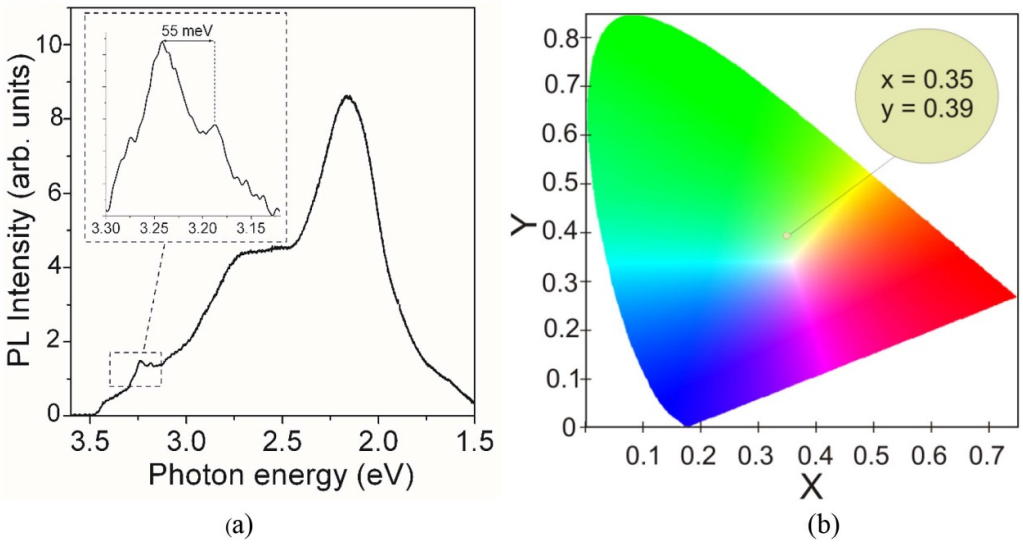

Figure 4. Room-temperature PL spectrum of ZnO nanocrystals in silica (a) and colour space chromaticity CIE-1931 diagram (b) showing the RT emission colour by circle.

the annealing regime used in our experiment, the emission at 2.3–2.8 eV can be attributed to various types of oxygen vacancies. The strong emission at 1.9–2.2 is usually associated with excess oxygen as a consequence of oxygen-rich ZnO growth conditions or annealing in oxygen atmosphere [31, 34] and commonly attributed to oxygen interstitial (O_i) defects [31, 36] or Zn vacancies [37, 38]. In our experiment, the additional oxygen implantation is most probably responsible for the creation of such defects.

Ion implantation is always accompanied by the formation of defects in the silica matrix [39]. Therefore, the RT luminescence can also originate from the silica matrix mainly by optically active defects [30, 40]. There are different types of oxygen-deficiency-related centres (ODC). In particular, the twofold coordinated silicon = Si••, may be responsible for emission at 2.7–2.8 eV via triplet-singlet transitions [30, 31, 38, 39]. Also, the origin of the emission at 2.6–2.8 eV can be explained via formation of self-trapped excitons (electron–hole pairs made of a peroxy linkage and an E' centre (≡Si•)). An emission in the visible spectral range of (1.85–1.95 eV) is unambiguously attributed to non-bridging oxygen hole centres (NBOHC) (≡Si–O•) [31, 39–41]. All of the above-mentioned intrinsic silica defects can contribute to light emission of the synthesised nanocomposite. However, taking into account the conditions of PL excitation and post-implantation annealing, we can expect that the contribution of ZnO NCs dominates in PL emission. First, the energy of the He–Cd laser (3.81 eV) used in our experiment is not sufficient for effective excitation of optical active defects in silica. Under 3.81 eV excitation, only a low-intensity luminescence should be observed. To excite intrinsic defects in silica, electron beam (cathodoluminescence), γ-irradiation [30, 39] or excimer lasers [42] are usually used. Second, based on results presented in [43], a high concentration of ODCs as well as NBOHCs is not to be expected after annealing at 750 °C for 120 min in air. Contrary, the energy of the excitation laser line (3.81 eV) provides a near-resonant excitation condition for ZnO because it is close to the ZnO band gap. Thus, we can suggest that the radiative recombination in ZnO NCs is the main mechanism of light emission in our nanocomposite ZnO NCs in silica.

The appearance of ZnO NBE bands in the RT PL spectrum (figure 4) already indicates a good crystal quality of the synthesised NCs. The intensive emission in the visible spectral range favours such structures as promising materials for modern optoelectronic devices (for example white nano LED's). In this regard, the RT PL spectrum of the synthesised structure was transposed to the CIE-1931 standard, as shown in figure 4(b). The chromatic coordinate of the observed white with a greenish tint emission is (0.35, 0.39) which is close to the standard white light (0.333, 0.333) coordinates. Thus, the formed structure with ZnO NCs in silica can be very useful for high-performance optoelectronic device applications.

To verify and clarify the origin of the observed emission and estimate the contribution of impurity bound excitons and defects, low-temperature PL measurements were carried out. Figure 5 shows the PL spectrum measured over a broad spectral range. In contrast to the RT PL spectrum, the UV emission of ZnO dominates the PL spectrum registered at 4 K, as the intensity of the ZnO NBE emission can easily increase by several orders of magnitude with decreasing temperature, whereas for silica this would by only a factor of 2 in the spectral range investigated [30]. Similar as in the RT PL spectrum, the ZnO NBE emission is composed of two distinct narrow lines at 3.324 and 3.274 eV generated from different transition processes. However, in the case of LT PL the intensities of these bands are comparable. The position of the NBE band is blue-shifted ($\Delta E \sim 80$ meV) due to the thermal bandgap-expanding effect with temperature decrease. Taking into account the energetic position and full width at a half maximum, the observed intense band at 3.324 eV can be attributed to the recombination of excitons bonded to donors (DBX). The shoulder on the short wavelength side at ∼3.35 eV can be assigned to

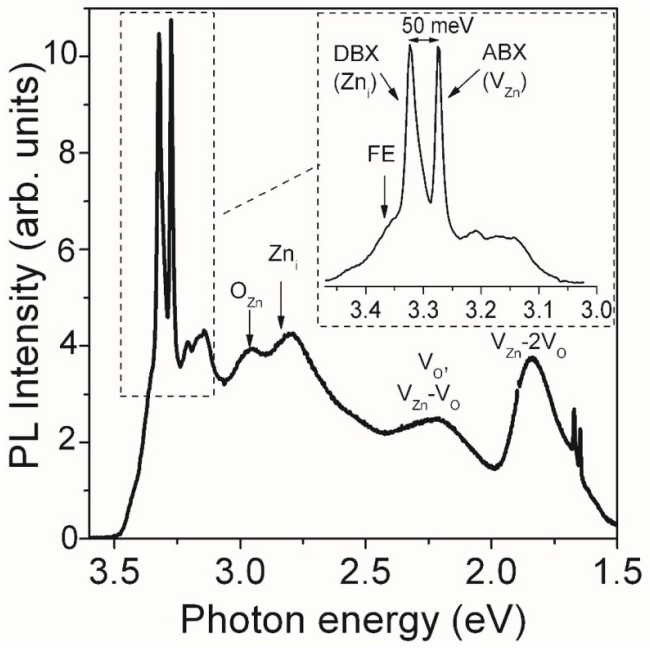

Figure 5. Low-temperature PL spectrum of ZnO nanocrystals in silica measured at 4 K. The inset shows the UV signal in more detail.

a free exciton (FE) recombination. Taking this into account, the donor-exciton localization energy (E_{loc}) is 26 meV. The second peak in the NBE range with maximum at 3.274 eV is most intriguing. The energy distance of this peak from the DBX line is only 50 meV. Hence, it cannot be the phonon replica, because this energy difference is less than the energy of the LO optical phonon in ZnO. In [6] two similar bands were registered in the NBE range for ZnO NCs synthesised by implantation of ZnO^+ molecular ions into silica. These bands were attributed to donor and ABXs without mentioning a possible nature of the supposed defects. Also, the same low-temperature PL spectrum shape has been demonstrated for a polycrystalline ZnO film disordered by 700 keV oxygen ion irradiation [44]. In [44] the origin of the observed bands was discussed in detail. According to [44] the bands registered at 3.324 and 3.274 eV in our experiment can be assigned to donor and ABXs, respectively. First-principle studies of intrinsic point defects in zinc oxide [45–47] reveal that Zn interstitials (Zn_i), oxygen vacancies (V_O) and antisite defects (Zn_O) act as donor defects, while Zn vacancies (V_{Zn}) and oxygen interstitials (O_i) act as acceptors. It should be noted that the zinc interstitial has the lowest formation energy among these intrinsic defects, so it should be the dominant donor in zinc oxide.

The LT PL spectrum for the here synthesised structure exhibits a number of bands in the visible spectral range with maxima at 2.95, 2.79, 2.22 and 1.84 eV (figure 5). According to [31, 33, 35–37, 44, 48–50], we can interpret the bands as follows. The band at 2.95 eV can be related to antisite defects (O_{Zn}), while the band at 2.79 eV can be ascribed to Zn interstitials (Zn_i). The band at 2.22 eV can be attributed to oxygen interstitials (O_i), zinc vacancies, as well as oxygen vacancies (single ionised) and divacancies V_{Zn}–V_O. The band at 1.84 eV can be assigned to the complex V_{Zn}–$2V_O$. Thus, taking into account the complicated structure of the composite of ZnO NCs in SiO_2, it is difficult to give an exact interpretation of the PL spectrum. But we can state that there are different centres of radiative recombination in ZnO NCs synthesised in silica by ion implantation.

Another important point to note is the negative thermal quenching of the defect emission. The intensity of the emission at 1.9–2.7 eV (especially at 2.16 eV) increases as the temperature increases, while the NBE emission decreases. A similar tendency is observed in [51–53]. The explanation of the activation of defect-induced emission with increasing temperature is that thermally activated excitons can be re-trapped by the defects.

Thus, different trap states due to both donors and acceptors are involved in the light emission of the synthesised nanostructure. Such a diversity of defect-related recombination centres for undoped NCs can be explained by special features of the process of ion beam synthesis. First of all, ion implantation is a non-equilibrium process. It is known that native defects (such as oxygen interstitials and oxygen antisites) have high formation energies and, therefore, are not expected to play a role in carrier recombination in ZnO prepared under near equilibrium conditions [54]. In the case of ion beam synthesis, the formation of such type of defects is quite expectable. Furthermore, ion-induced defects are formed within the clusters synthesised during implantation. Post-implantation thermal treatment may be not sufficient to eliminate them. So, the chosen annealing temperature in our experiment (750 °C) is not sufficient to eliminate Zn vacancies, as it was shown in [35]. Second, there is also an effect of the silica matrix. Namely, the high interface area of ZnO precipitates in the SiO_2 matrix creates defect levels (mainly a large number of acceptor-type defects near the interface) that support the defect emission [55]. Additionally, here we observe the formation of core/shell structures. Therefore, oxygen vacancies (V_O, $2V_O$) can be located at the interface between the ZnO shell and the Zn core, while zinc vacancies (V_{Zn}) are located at the interface ZnO shell/SiO_2 matrix. Thus, more complex defects such as V_{Zn}–V_O and V_{Zn}–$2V_O$ are expected to be involved in the radiative recombination even at low temperature.

4. Conclusions

In summary, zinc blende ZnO NCs have been synthesised in a silica matrix by dual (Zn, O) ion implantation with subsequent annealing at 750 °C for 120 min in air ambient. Besides ZnO nanoclusters, the formation of core/shell nanoclusters (most probably Zn core/ZnO shell) has been revealed. The synthesised nanocomposite exhibits strong white-greenish emission in a broad visible spectral range at room temperature. The origin of this emission is mainly associated with the synthesised NCs and to a much lesser extend with defects in silica. The emission intensity is higher at room temperature than at low temperature that makes such a structure very attractive for silicon photonics. Based on the data of low temperature PL spectroscopy, it has been shown that intrinsic defects with

donor and acceptor characteristics play a crucial role in the emission mechanisms in both the UV (bound exciton) and visible spectral range. Thus, the main recombination processes in ion-beam synthesised zb-ZnO NCs involve donor as well as acceptor levels. This fact represents an additional crucial point which has to be taken into account when discussing the potential application of ZnO-based nanoscale optoelectronic devices.

Data availability statement

All data that support the findings of this study are included within the article (and any supplementary files).

Acknowledgments

This work was partly supported by the Belarusian Republican Foundation for Fundamental Research (Grant No. T19RM-041) and Ministry of Education and Science of the Russian Federation in the framework of Increase competitiveness program of NUST 'MISIS'. The authors acknowledge the support of exchange of scientists by Erasmus+ of the EU.

ORCID iD

E Wendler https://orcid.org/0000-0001-5325-298X

References

[1] Shastri L, Qureshi M S and Malik M M 2013 *J. Phys. Chem. Solids* **74** 595
[2] Barhoum A, Van Assche G, Rahier H, Fleisch M, Bals S, Delplancked M-P, Leroux F and Bahnemann D 2017 *Mater. Des.* **119** 270
[3] Thiyagarajan P, Kottaisamy M, Ramaa N and Ramachandra Rao M S 2008 *Scr. Mater.* **59** 722
[4] Ma J G, Liu Y C, Xu C S, Liu Y X, Shao C L, Xu H Y, Zhang J Y, Lu Y M, Shen D Z and Fan X W 2005 *J. Appl. Phys.* **97** 103509
[5] Zhong K 2013 *Spectrosc. Lett.* **46** 160
[6] Pandey B, Poudel P R, Singh A K, Neogi A and Weathers D L 2013 *Appl. Phys.* A **112** 801
[7] Privezentsev V V, Kulikauskas V S, Zatekin V V, Zinenko V I, Agafonov Y A, Egorov V K, Steinmand E A, Tereshchenkod A N and Shcherbacheve K D 2019 *J. Surf. Invest.* **13** 382
[8] Amekura H, Okubo N, Ren F and Ishikawa N 2018 *J. Appl. Phys.* **124** 145901
[9] Mayer M 2014 *Nucl. Instrum. Methods Phys. Res.* B **332** 176
[10] Ziegler J F, Ziegler M D and Biersack J P 2010 *Nucl. Instrum. Methods Phys. Res.* B **268** 1818
[11] Geburt S 2013 Lasing and ion beam doping of semiconductor nanowires PhD Thesis University of Jena, Germany
[12] Özgür Ü, Alivov Y I, Liu C, Teke A, Reshchikov M A, Doğan S, Avrutin V, Cho S-J and Morkoç H 2005 *J. Appl. Phys.* **98** 041301
[13] Karzel H, Potzel W, Köfferlein M, Schiessl W, Steiner M, Hiller U and Kalvius G M 1996 *Phys. Rev.* B **53** 11425
[14] Ashrafi A and Jagadish C 2007 *J. Appl. Phys.* **102** 071101
[15] Dauletbekova A, Vlasukova L, Baimukhanov Z, Akilbekov A, Kozlovskyi A, Giniyatova S, Seitbayev A, Usseinov A and Akylbekova A 2019 *Phys. Status Solidi* b **256** 1800408
[16] Amekura H, Tanaka M, Katsuya Y, Yoshikawa H, Ohnuma M, Matsushita Y, Kobayashi K and Kishimoto N 2010 *J. Appl. Phys.* **108** 104302
[17] Campbell C T 1997 *Surf. Sci. Rep.* **27** 1–111
[18] Mahapatra A K, Bhatta U M and Som T 2012 *J. Phys. D: Appl. Phys.* **45** 415303
[19] Muñoz-Aguirre N, Martínez-Pérez L, Muñoz-Aguirre S, Armando Flores-Herrera L, Vergara Hernández E and Zelaya-Ange O 2019 *Materials* **12** 3314
[20] Zagorac D, Schön J C, Zagorac J and Jansen M 2014 *Phys. Rev.* B **89** 075201
[21] Sun X W, Liu Z J, Chen Q F, Lua H W, Song T and Wang C W 2006 *Solid State Commun.* **140** 219–24
[22] Karazhanov S, Ravindran P, Kjekshus A, Fjellvag H and Svensson B 2007 *Phys. Rev.* B **75** 155104
[23] Martínez-Pérez L, Muñoz-Aguirre N, Muñoz-Aguirre S and Zelaya-Angel O 2015 *Mater. Lett.* **139** 63–5
[24] Zhou S-M, Gong H-C, Zhang B, Du Z-L, Zhang X-T and Wu S-X 2008 *Nanotechnology* **19** 175303
[25] Lee G H, Kawazoe T and Ohtsu M 2005 *Appl. Surf. Sci.* **239** 394
[26] Yoo Y-Z, Osaka Y, Fukumura T, Kawasaki M, Koinuma H, Chikyow T, Ahmet P, Setoguchi A and Chichibu S F 2001 *Appl. Phys. Lett.* **78** 616
[27] Hamby D W, Lucca D A, Kolpfstein M J and Cantwell G 2003 *J. Appl. Phys.* **93** 3214
[28] Oshikiri M and Aryasetiawan F 1999 *Phys. Rev.* B **60** 10754
[29] Zahn D R T, Maierhofer C, Winter A, Reckzügel M, Srama R, Rossow U, Thomas A, Horn K and Richter W 1992 *Appl. Surf. Sci.* **56–58** 684–90
[30] Kaidashev V E, Kaidashev E M, Misochko O V, Maksimuk M Y, Fursova T N and Bazhenov A V 2009 *Bull. Russ. Acad. Sci.* **73** 1528–31
[31] Shang N G, Vetter U, Gerhards I, Hofsäss H, Ronning C and Seibt M 2006 *Nanotechnology* **17** 3215
[32] Shen Y, Li Z, Zhang X, Zhang D, He W, Xue Y, Gao Y, Zhang X, Wang Z and Liu C 2010 *Opt. Mater.* **32** 961
[33] Tam K H *et al* 2006 *J. Phys. Chem.* B **110** 20865
[34] Vempati S, Mitra J and Dawson P 2012 *Nanoscale Res. Lett.* **7** 470
[35] Thapa D, Huso J, Morrison J L, Corolewski C D, McCluskey M D and Bergman L 2016 *Opt. Mater.* **58** 382
[36] Kocsis K, Janotti A and Van De Walle C G 2006 *J. Cryst. Growth* **287** 58
[37] McCluskey M D, Corolewski C D, Lv J, Tarun M C, Teklemichael S T, Walter E D, Norton M G, Harrison K W and Ha S 2015 *J. Appl. Phys.* **117** 112802
[38] Knutsen K E, Galeckas A, Zubiaga A, Tuomisto F, Farlow G C, Svensson B G and Kuznetsov A Y 2012 *Phys. Rev.* B **86** 121203(R)
[39] Salh R 2011 Defect related luminescence in silicon dioxide network: a review *Crystalline Silicon—Properties and Uses* ed S Basu (Rijeka: InTech) ch 8 pp 135–72
[40] Skuja L 1998 *J. Non-Cryst. Solids* **239** 16–48
[41] Gritsenko V A, Novikov Y N, Shaposhnikov A and Morokov Y N 2001 *Semiconductors* **35** 997–1005
[42] Trukhin A N 2019 *J. Non-Cryst. Solids* **521** 119525
[43] Griscom D L 1991 Optical properties and structure of defects in silica glass *J. Ceramic Soc. Japan* **99** 923–42
[44] Pal S, Rakshit T, Singha S S, Asokan K, Dutta S, Jana D and Sarkar A 2017 *J. Alloys Compd.* **703** 26
[45] Erhart P, Albe K and Klein A 2006 *Phys. Rev.* B **73** 205203
[46] Kohan A F, Ceder G, Morgan D and Van de Walle C G 2000 *Phys. Rev.* B **61** 15019
[47] Oba F, Nishitani S R, Isotani S and Adachi H 2001 *J. Appl. Phys.* **90** 824
[48] Cao B, Cai W and Zeng H 2006 *Appl. Phys. Lett.* **88** 161101
[49] Zeng H, Duan G, Li Y, Yang S, Xu X and Cai W 2010 *Adv. Funct. Mater.* **20** 561

[50] Ye J D *et al* 2005 *Appl. Phys.* A **81** 759–62
[51] Zhou J, Nomenyo K, Cesar C C, Lusson A, Schwartzberg A, Yen C-C, Woon W-Y and Leronde G 2020 *Sci. Rep.* **10** 4237
[52] Lin S S, Chen B G, Xiong W, Yang Y, He H P and Luo J 2012 *Opt. Express* **20** A706-12
[53] Shan C X, Liu Z and Hark S K 2008 *Appl. Phys. Lett.* **92** 073103
[54] Janotti A and Van de Walle C G 2009 *Rep. Prog. Phys.* **72** 126501
[55] Fonoberov V A, Alim K A, Balandin A A, Xiu F and Liu J 2006 *Phys. Rev.* B **73** 165317